Supplementary Material to the article "Effect of local electric field and dipole-dipole interaction on spontaneous dipole moment order in orthorhombic bismuth monolayers"

S1. ESTIMATE OF BISMUTH ATOM POLARIZABILITIES IN ORTHOROMBIC MONOLAYERS FROM FIRST PRINCIPLES

First-principles calculations were carried out within the density functional theory (DFT) formalism implemented in the Vienna Ab-initio Simulation Package (VASP) [1, 2]. Local density (LDA) [3] and general gradient (GGA-PBE) [4] approximations were used for exchange-correlation functional with a projector augmented-wave pseudopotentials [5], treating the Bi 6s 6p as valence electrons. The plane-wave energy cutoff was 550 eV. Convergence achieved when the total energy change between steps is less than 10^{-7} eV. A dipole correction [6] was applied for account of homogeneous external electric field. Spin-orbit coupling (SOC) effect was not included in all calculations. In all calculations we used experimental values of lattice parameters [7] $a = 4.75$ Å, $b = 4.42$ Å, and $d = 2.8$ Å.

We determine atomic polarizability tensors, $\alpha_{ij}^{(s)}$, for atoms occupying each sublattice $s = 1, 2, 3, 4$ with the help of the following indentity:

$$p_i^{(s)} = \alpha_{ij}^{(s)} E_j^{(s)}, \tag{S1}$$

where $p_i^{(s)}$ is i-th ($i = x, y, z$) component of atomic dipole moment for sublattice induced by the j-th component of local electric field $E_j^{(s)}$. Polarizability of each sublattices is calculated dividing monolayer unit cells into four Voronoi cells (VC) centered at the position $\boldsymbol{\tau}_s$ in such a way that sum of VC volumes equals unit cell volume and

$$\int_{\mathrm{VC_s}} \left[\rho_{\mathbf{E}^{\mathrm{ext}}}(\boldsymbol{r}) - \rho_0(\boldsymbol{r})\right] d^3r = 0, \quad s = 1, 2, 3, 4, \tag{S2}$$

where $\rho_{\mathbf{E}^{\mathrm{ext}}}(\boldsymbol{r})$ and $\rho_0(\boldsymbol{r})$ are electron densities computed in DFT at finite and zero external electric field, respectively. Then, the dipole moments of atoms in a unit cell are evaluated as follows:

$$\boldsymbol{p}^{(s)} = \int_{\mathrm{VC_s}} \left[\rho_{\mathbf{E}^{\mathrm{ext}}}(\boldsymbol{r}) - \rho_0(\boldsymbol{r})\right] \boldsymbol{r} d^3r. \tag{S3}$$

Local electric field, $E_j^{(s)}$ were determined in different ways for in-plane and out-of-plane orientations of applied external field. For the in-plane direction of external field, we determined the local field via slope of total potential difference, $\varphi_{\mathbf{E}^{\mathrm{ext}}} - \varphi_0$ (shown in Fig. S1), computed with finite, $\varphi_{\mathbf{E}^{\mathrm{ext}}}$, and zero, φ_0, external fields, for nanoribbons of width 88.4 Å (for $Ox||$ armchair axis) and 99.4 Å (for $Oy||$ zigzag axis) with in-plane vacuum gaps between periodic images being 22.1 Å and 19.3 Å, respectively, and

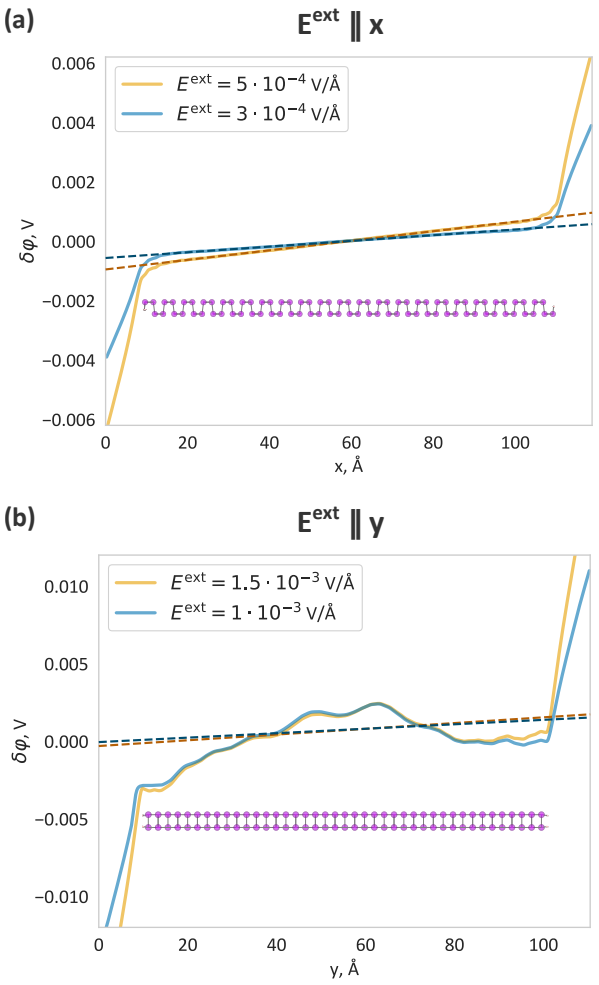

FIG. S1. Planar averaged potential difference $\delta\varphi = \varphi_{\mathbf{E}^{\mathrm{ext}}} - \varphi_0$ for $\mathbf{E}^{\mathrm{ext}}||Ox$ (a) and $\mathbf{E}^{\mathrm{ext}}||Oy$ (b). The dashed lines indicate fits of slopes for the potential that were used to estimate local fields in VC for each sublattice. The insets schematically show the corresponding nanoribbon geometries.

out-of-plane gaps 20 Å. Note, that cutting bismuth ribbons from monolayer leads to undesirable metallic edge states in the gap. Therefore, to eliminate the edge states from the gap of bismuth ribbons we passivated them with hydrogen atoms that positions were relaxed until convergence between steps of total energy were less than 10^{-6} eV and the forces acting on atoms were less than 10^{-3} eV/Å. The relaxed distances of Bi–H bond were 1.84 Å and 1.85 Å for nanoribbons with armchair and zigzag edges, respectively.

For out-of-plane direction of $\mathbf{E}^{\mathrm{ext}}||Oz$ we calculated the

local field as follows:

$$E_j^{(s)} = \frac{-\int_{\mathrm{VC}_s} \frac{\partial}{\partial x_j}\left[\varphi_{E_z^{\mathrm{ext}}} - \varphi_0 - \int \frac{(\rho_{E_z^{\mathrm{ext}}}(\boldsymbol{r}') - \rho_0(\boldsymbol{r}'))}{|\boldsymbol{r}-\boldsymbol{r}'|} d^3\boldsymbol{r}'\right] \rho_0(\boldsymbol{r})\, d^3\boldsymbol{r}}{\int_{\mathrm{VC}_s} \rho_0(\boldsymbol{r})\, d^3\boldsymbol{r}}, \quad \text{(S4)}$$

where the last term in square brackets on the right-hand side excludes electric field produced by the electron density inside its VC (i. e. self-action).

For $\mathbf{E}^{\mathrm{ext}}$ along armchair ($||x$), zigzag ($||y$) and out-of-plane directions the Brillouin zone integration for corresponding primitive cells was performed on k-point grids of $11\times1\times1$, $1\times11\times1$, and $11\times11\times1$, respectively.

As a result we obtained the following values for polarizability tensors (in Å^3):

$$\alpha_{ij}^{(1)} = \begin{pmatrix} 6.7 & -0.4 & -0.4 \\ 0.3 & 7.8 & 0.1 \\ -1.4 & 4.8 & 6.4 \end{pmatrix}, \quad \text{(S5)}$$

$$\alpha_{ij}^{(2)} = \begin{pmatrix} 6.7 & 0.4 & 0.4 \\ -0.3 & 7.8 & 0.1 \\ -1.4 & 4.8 & 6.4 \end{pmatrix}, \quad \text{(S6)}$$

$$\alpha_{ij}^{(3)} = \begin{pmatrix} 6.7 & -0.4 & 0.4 \\ 0.3 & 7.8 & -0.1 \\ 1.4 & -4.8 & 6.4 \end{pmatrix}, \quad \text{(S7)}$$

$$\alpha_{ij}^{(4)} = \begin{pmatrix} 6.7 & 0.4 & -0.4 \\ -0.3 & 7.8 & -0.1 \\ 1.4 & -4.8 & 6.4 \end{pmatrix}. \quad \text{(S8)}$$

CALCULATION OF BORN EFFECTIVE CHARGES

The Born effective charge tensors $Z_{ij}^{(s)}$ were calculated within DFT. The exchange–correlation interaction was described by the GGA–PBE functional. The plane-wave energy cutoff is 600 eV. The Brillouin zone of the primitive monolayer cell was sampled with a $24\times24\times1$ k-point mesh. The energy convergence criterion was 10^{-9} eV.

The obtained Born charge tensors for the four sublattices are (components are in units of the elementary charge e):

$$Z_{ij}^{(1)} = Z_{ij}^{(4)} = \begin{pmatrix} 0.00 & 0.00 & -1.49 \\ 0.00 & 0.00 & 0.00 \\ -0.03 & 0.00 & 0.00 \end{pmatrix}, \quad Z_{ij}^{(2)} = Z_{ij}^{(3)} = \begin{pmatrix} 0.00 & 0.00 & 1.49 \\ 0.00 & 0.00 & 0.00 \\ 0.03 & 0.00 & 0.00 \end{pmatrix}. \quad \text{(S9)}$$

S2. CALCULATION OF LATTICE SUMS

We calculate lattice sum in equation (2) of the main text as follows:

$$S_{ss'} = {\sum_n}' \frac{e^{-i\boldsymbol{q}(\boldsymbol{R}_n+\boldsymbol{\tau}_{ss'})}}{|\boldsymbol{r}-(\boldsymbol{R}_n+\boldsymbol{\tau}_{ss'})|} = \sum_n \frac{2}{\sqrt{\pi}} \int_0^{+\infty} e^{-i\boldsymbol{q}(\boldsymbol{R}_n+\boldsymbol{\tau}_{ss'})} e^{-|\boldsymbol{r}-(\boldsymbol{R}_n+\boldsymbol{\tau}_{ss'})|^2\eta^2} d\eta. \quad \text{(S10)}$$

For $(s,s') = (1,3),(1,4),(2,3),(2,4)$, $\tau_{z,ss'} \neq 0$ and making Fourier transform in eq. (S10) we obtain

$$S_{ss'} = \sum_{\boldsymbol{G}_m} \frac{2\pi}{\Omega_0 |\boldsymbol{G}_m - \boldsymbol{q}|} e^{i(\boldsymbol{G}_m-\boldsymbol{q})\boldsymbol{r} - i\boldsymbol{G}_m\boldsymbol{\tau}_{ss'} - |\boldsymbol{G}_m-\boldsymbol{q}||z-\tau_{z,ss'}|}, \quad \text{(S11)}$$

which rapidly converges due to $e^{-G_m|\tau_{z,ss'}|}$.

For $(s,s') = (1,2),(3,4)$ $\boldsymbol{\tau}_{ss'} = (\boldsymbol{\tau}_{||,ss'},0)$, so that we divide integration range by η_0, which leads to the following:

$$\begin{aligned} S_{ss'} &= \sum_n \frac{2}{\sqrt{\pi}} \int_0^{+\infty} e^{-i\boldsymbol{q}(\boldsymbol{R}_n+\boldsymbol{\tau}_{ss'})} e^{-|\boldsymbol{r}-(\boldsymbol{R}_n+\boldsymbol{\tau}_{ss'})|^2\eta^2} d\eta = \\ &\frac{2}{\sqrt{\pi}} \int_0^{\eta_0} \sum_n e^{-i\boldsymbol{q}(\boldsymbol{R}_n+\boldsymbol{\tau}_{||,ss'})} e^{-\left|\boldsymbol{r}-\boldsymbol{R}_n-\boldsymbol{\tau}_{||,ss'}\right|^2\eta^2} d\eta + \\ &+ \frac{2}{\sqrt{\pi}} \int_{\eta_0}^{\infty} \sum_n e^{-i\boldsymbol{q}(\boldsymbol{R}_n+\boldsymbol{\tau}_{||,ss'})} e^{-\left|\boldsymbol{r}-\boldsymbol{R}_n-\boldsymbol{\tau}_{||,ss'}\right|^2\eta^2} d\eta = \\ &= \frac{2\pi}{\Omega_0} \sum_{\boldsymbol{G}_m} e^{-i\boldsymbol{G}_m\boldsymbol{\tau}_{||,ss'} + i(\boldsymbol{G}_m-\boldsymbol{q})\boldsymbol{r}} \frac{\mathrm{erfc}\left(\frac{|\boldsymbol{G}_m-\boldsymbol{q}|}{2\eta_0}\right)}{|\boldsymbol{G}_m-\boldsymbol{q}|} + \\ &+ \sum_n \frac{e^{-i\boldsymbol{q}(\boldsymbol{R}_n+\boldsymbol{\tau}_{||,ss'})} \mathrm{erfc}(\eta_0 \left|\boldsymbol{r}-\boldsymbol{R}_n-\boldsymbol{\tau}_{||,ss'}\right|)}{\left|\boldsymbol{r}-\boldsymbol{R}_n-\boldsymbol{\tau}_{||,ss'}\right|}, \end{aligned} \quad \text{(S12)}$$

Finally for the case $s = s'$ we obtain:

$$\begin{aligned} S_{ss} &= \sum_n \frac{e^{-i\boldsymbol{q}\boldsymbol{R}_n}}{|\boldsymbol{r}-\boldsymbol{R}_n|} - \frac{1}{|\boldsymbol{r}|} = \\ &= \sum_n \frac{2}{\sqrt{\pi}} \int_0^{+\infty} e^{-i\boldsymbol{q}\boldsymbol{R}_n} e^{-|\boldsymbol{r}-\boldsymbol{R}_n|^2\eta^2} d\eta - \frac{1}{|\boldsymbol{r}|} = \\ &= \frac{2}{\sqrt{\pi}} \int_0^{\eta_0} \sum_n e^{-i\boldsymbol{q}\boldsymbol{R}_n} e^{-|\boldsymbol{r}-\boldsymbol{R}_n|^2\eta^2} d\eta + \\ &+ \frac{2}{\sqrt{\pi}} \int_{\eta_0}^{\infty} \sum_n e^{-i\boldsymbol{q}\boldsymbol{R}_n} e^{-|\boldsymbol{r}-\boldsymbol{R}_n|^2\eta^2} d\eta - \frac{1}{|\boldsymbol{r}|} = \\ &= \frac{2\sqrt{\pi}}{\Omega_0} \sum_{\boldsymbol{G}_m} e^{i(\boldsymbol{G}_m-\boldsymbol{q})\boldsymbol{r}} \int_0^{\eta_0} \frac{1}{\eta^2} e^{-\eta^2 z^2 - \frac{|\boldsymbol{G}_m-\boldsymbol{q}|^2}{4\eta^2}} d\eta + \\ &+ \sum_{n\neq0} \frac{e^{-i\boldsymbol{q}\boldsymbol{R}_n} \mathrm{erfc}(\eta_0 |\boldsymbol{r}-\boldsymbol{R}_n|)}{|\boldsymbol{r}-\boldsymbol{R}_n|} - \frac{2\eta_0}{\sqrt{\pi}}. \end{aligned} \quad \text{(S13)}$$

Both sums in eqs. (S12) and (S13) are rapidly converged with a proper choice of η_0.

S3. COMPARISON OF PHONON SPECTRA IN DFT AND THE NEAREST NEIGHBOUR APPROXIMATION

Lattice dynamics calculations were performed with the Phonopy package [8, 9]. The force constants were obtained from a $3\times3\times1$ supercell of the bismuth monolayer using GGA-PBE approximation with the plane wave cutoff 600 eV, $8\times8\times1$ Monkhorst-Pack k-point mesh [10] and energy convergence criterion 10^{-9}.

In Fig. S2 we display all phonon branch dispersions obtained with the help of dynamical matrix in the nearest neighbour approximation for force constants from Table S1 in the main text (left panel) and that of Phonopy package (right panel) [8, 9], which are in a good quantitative agreement. In both cases we used the experimental lattice parameters.

S4. STABILITY OF PHONON SPECTRA FOR NON-POLAR ORTHORHOMBIC BISMUTH LATTICE

We find (see Fig. S3) that in the nearest neighbor approximation model with experimental lattice parameters to obtain stability for ZO optical branch (which also produces stabile dispersion for ZA branch) it is enough to change sign of Φ^{12}_{zz}, compared to the initial DFT-obtained values, which also inflicts small change of Φ^{14}_{zz}, due to identity $\Phi^{14}_{zz}+\Phi^{11}_{zz}+2\Phi^{12}_{zz}=0$. In addition, 5% decrease of Φ^{12}_{xy} makes real frequency for the chiral (C) mode in M point. Nevertheless, account of dipole-dipole interaction results in imaginary frequency for optical ZO mode, see Fig. S3(b).

TABLE S1. Corrected values of parameters (highlighted by bold) of dynamical matrix (eV/Å^2) for stability of phonon spectra without dipole-dipole interaction.

	xx	yy	zz	$xz/xy/yz$
Φ^{11}	8.348	11.505	9.1309	1.689 (xz)
Φ^{12}	-3.74	-5.22	**-0.409**	**4.313** (xy), -0.13 (yz)
Φ^{14}	-0.868	-1.065	**-8.321**	—

S5. PHONON SPECTRA IN FERROELECTRIC PHASE OF ORTHORHOMBIC BISMUTH MONOLAYERS

In Fig. S4(a) we find optimal value of ZO mode amplitude, $h_0 = 0.94$ Å, that provides gain in energy for the ferroelectric phase orthorhombic bismuth monolayers with respect to the non-polar lattice with experimental lattice parameters $a = 4.75$ Å, $b = 4.42$ Å, and $d = 2.8$ Å. Calculated in DFT phonon spectra (Fig. S4(b)) with $3\times3\times1$ and $4\times4\times1$ supercells show that lattice structure of the ferroelectric phase is stable, as all optical phonons possess positive energies, whereas small imaginary values for acoustic phonons near Γ point are attributed to numerical accuracy related to supercell sizes [11].

[1] G. Kresse and J. Hafner, "Ab initio molecular dynamics for liquid metals", Physical review B **47**, 558 (1993).

[2] G. Kresse and J. Furthmüller, "Efficient iterative schemes for *ab initio* total-energy calculations using a plane-wave basis set", Physical Review B **54**, 11169 (1996).

[3] D. M. Ceperley and B. J. Alder, "Ground state of the electron gas by a stochastic method", Physical Review Letters **45**, 566 (1980).

[4] J. P. Perdew, K. Burke, and M. Ernzerhof, "Generalized gradient approximation made simple", Physical Review Letters **77**, 3865 (1996).

[5] P. E. Blöchl, "Projector augmented-wave method", Physical Review B **50**, 17953 (1994).

[6] J. Neugebauer and M. Scheffler, "Adsorbate-substrate and adsorbate-adsorbate interactions of Na and K adlayers on al(111)", Phys. Rev. B **46**, 16067 (1992).

[7] J. Gou, L. Kong, X. He, Y. L. Huang, J. Sun, S. Meng, K. Wu, L. Chen, and A. T. S. Wee, "The effect of moiré superstructures on topological edge states in twisted bismuthene homojunctions", Science advances **6**, eaba2773 (2020).

[8] A. Togo and I. Tanaka, "First principles phonon calculations in materials science", Scripta Materialia **108**, 1 (2015).

[9] A. Togo, "First-principles phonon calculations with Phonopy and Phono3py", Journal of the Physical Society of Japan **92**, 012001 (2023).

[10] H. J. Monkhorst and J. D. Pack, "Special points for brillouin-zone integrations", Physical Review B **13**, 5188 (1976).

[11] E. Aktürk, O. U. Aktürk, and S. Ciraci, "Single and bilayer bismuthene: Stability at high temperature and mechanical and electronic properties", Physical Review B **94**, 014115 (2016).

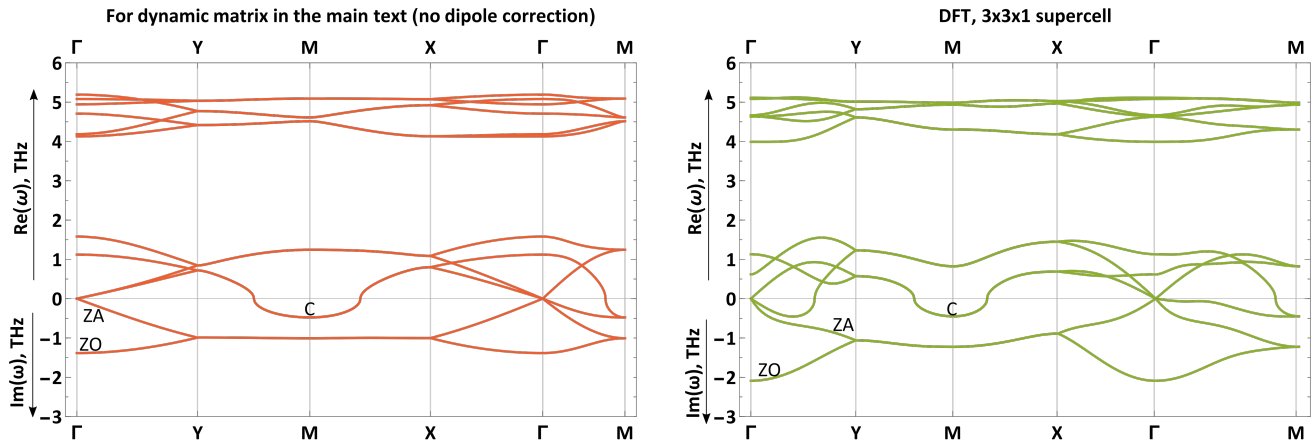

FIG. S2. Phonon spectra in orthorhombic bismuth monalayers obtained with dynamical matrix from the main text (left) (without account of dipole correction) and using the Phonopy package [8, 9] with 3x3x1 supercell (right).

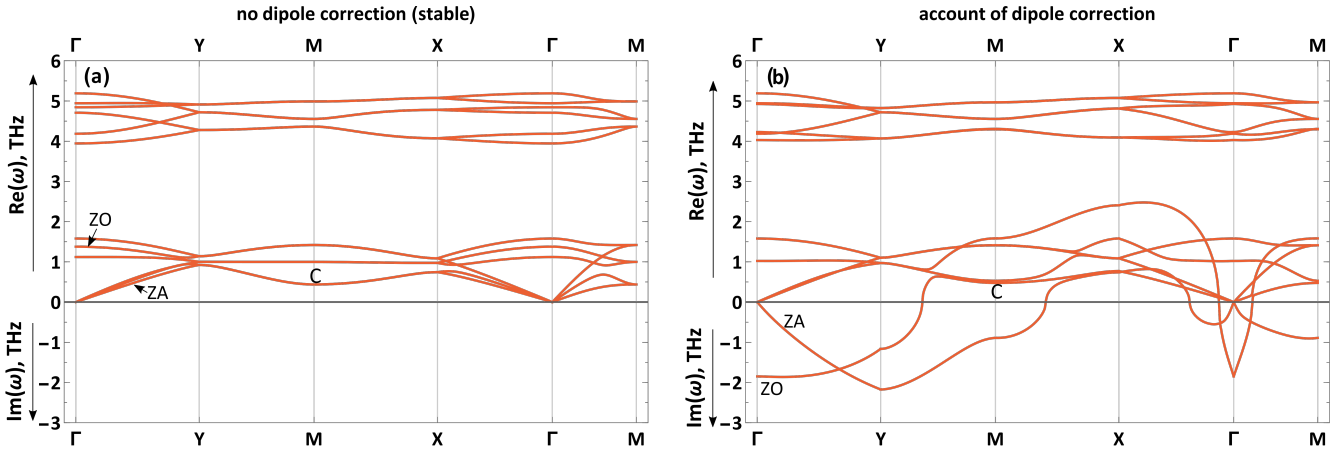

FIG. S3. (a) and (b) are phonon spectra in nonpolar (symmetric lattice) orthorhombic bismuth monolayers obtained for parameters listed in Table S1 without and with dipole-dipole interaction, respectively.

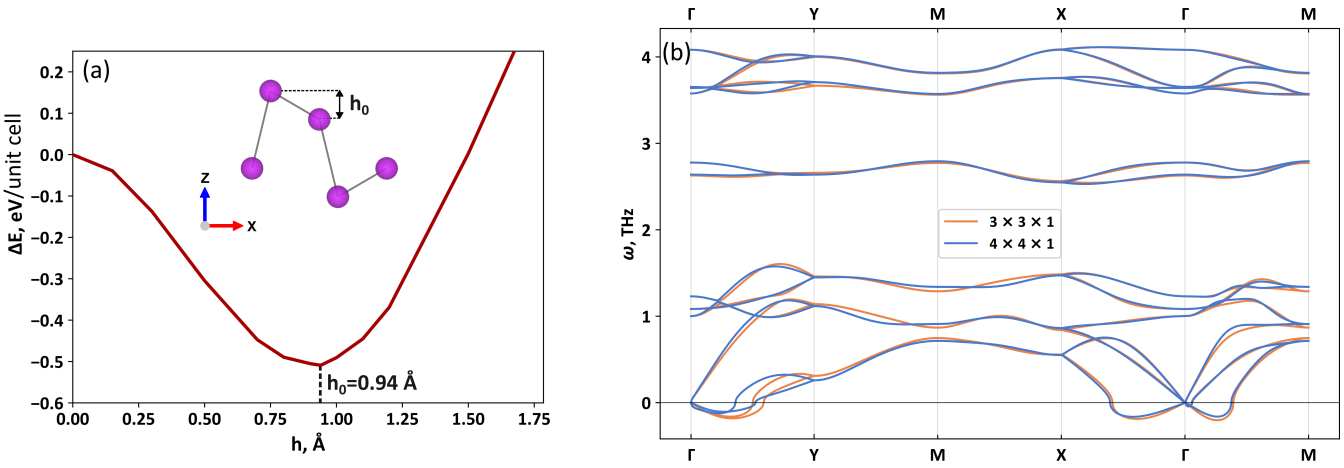

FIG. S4. (a) Energy difference per unit cell between ferroelectric and non-polar structures of orthorhombic bismuth monolayers. Inset shows unit cell in the ferroelectric phase. (b) Phonon spectra for ferroelectric orthorhombic bismuth monolayers (shown on inset on panel (a)), obtained for $3 \times 3 \times 1$ and $4 \times 4 \times 1$ supercells.